Computational study of elastic waves generated by ultrafast demagnetization in fcc Ni

I. Korniienko[1,*] P. Nieves[2] A. Fraile[3] R. Iglesias[2,4] and D. Legut[1,5]

[1]*IT4Innovations, VŠB - Technical University of Ostrava, 17. listopadu 2172/15, 70800 Ostrava-Poruba, Czech Republic*

[2]*Departamento de Física, Universidad de Oviedo, C. Leopoldo Calvo Sotelo, 18, 33007, Oviedo, Spain*

[3]*Material Physics Center (MPC)/Centro de Física de Materiales(CFM) CSIC-UPV/EHU, San Sebastián 20018, Spain*

[4]*Centro Universitario ASturias RAw Materials Institute (ASRAM), Universidad de Oviedo, C. Gonzalo Gutiérrez de Quirós, s/n, 33600, Mieres, Spain*

[5]*Department of Condensed Matter Physics, Faculty of Mathematics and Physics, Charles University, Ke Karlovu 3, 121 16 Prague 2, Czech Republic*

(Received 28 February 2024; revised 26 April 2024; accepted 1 May 2024; published 24 June 2024)

Picosecond ultrasonics is a fast growing and advanced research field with broad application to the imaging and characterization of nanostructured materials as well as at a fundamental level. The aim of this paper is to provide an advanced 3D model based on atomistic spin-lattice simulations of the laser-induced elastic response in ferromagnetically ordered fcc Ni. The advantage of such an approach is the possibility to take into account the laser radiation interaction with the spins and thus characterize the magnetic contribution to the total stress. We analyze the atomic displacements caused both by the ultrafast thermal expansion of the crystal lattice and by the demagnetization process due to the heating of a certain area of the sample by an ultrashort laser pulse. Subsequently, an attempt is made to propose mathematical expressions for describing the corresponding total stress. The lattice and magnetic contributions have been evaluated, whereupon the former is found to be much greater than the latter.

DOI: 10.1103/PhysRevResearch.6.023311

I. INTRODUCTION

With the development of ultrafast lasers, picosecond ultrasonics has become an advanced research field which nowadays shows great potential for elastic nanoscopy and ultrafast control of electronic and optical devices [1]. Using ultrafast lasers, it makes possible to generate and detect acoustic waves with frequencies up to terahertz and wavelengths down to nanometers and thus use picosecond laser ultrasonics to experimentally study nanostructures, adhesion of nanolayers, and profile inhomogeneity [2–4]. In particular, the usage of picosecond ultrasonics together with ultrashort x-ray probe pulses, a methodology discussed in Ref. [1], provides direct, layer-specific, and quantitative information on the picosecond strain response for structures down to few-nm thickness.

Impressive experimental achievements, however, face comparably limited theoretical descriptions and modeling of the laser-induced elastic response, both related to the complexity of the studied phenomenon. Thus, it is possible to construct analytical solutions for the strain field only for certain simplified cases [3,5]. As an alternative way, Mattern *et al.* [1] proposed the usage of numerical approaches by means of 1D linear chain models of masses and springs [6,7] to take into account the time dependence of the stresses by subsystem couplings, thermal diffusion, and interface effects. The situation becomes even more complicated in the case of using ferromagnetic materials due to the simultaneous magnetic degree of freedom interaction with the laser radiation [8,9] and coupling with the elastic degree of freedom. In other words, due to the laser-induced ultrafast demagnetization process [10–12], the magnetic subsystem can provide its own contribution to the elastic stress [13–15].

The aim of this paper is to perform an atom-resolved study on the basis of 3D atomistic spin-lattice simulations for laser-induced elastic response. As an example for testing our modeling approach, we use ferromagnetic fcc Ni. Such a choice allows us not only to calculate the lattice elastic response including ultrafast thermal expansion but also to characterize the magnetic contribution to stress in this material. Additional advantages of the 3D atomistic model include the ability to create more realistic structures with atomic resolution, defects, interfaces, given crystal orientations in layers, and the possibility to obtain the full strain and stress tensor components.

II. METHODOLOGY

A. Spin-lattice Hamiltonian

For the atomistic spin-lattice simulations, we consider the following Hamiltonian:

$$\mathcal{H}_{sl}(\mathbf{r},\mathbf{p},\mathbf{s}) = \mathcal{H}_{\mathrm{mag}}(\mathbf{r},\mathbf{s}) + \sum_{i=1}^{N}\frac{|\mathbf{p}_i|^2}{2m_i} + \sum_{i,j=1}^{N}\mathcal{V}(r_{ij}), \qquad (1)$$

where $\mathbf{r}_i$, $\mathbf{p}_i$, $\mathbf{s}_i$, and m_i stand for the position, momentum, normalized magnetic moment, and mass for each atom i in the

*Corresponding author: ievgeniia.korniienko@vsb.cz

system, respectively, $\mathcal{V}(r_{ij}) = \mathcal{V}(|\mathbf{r}_i - \mathbf{r}_j|)$ is the interatomic potential energy and N is the total number of atoms in the system with total volume V. In this paper, we restrict ourselves to elastic waves induced by exchange magnetostriction, so we only include the exchange interaction in the magnetic energy,

$$\mathcal{H}_{\text{mag}}(\mathbf{r}, \mathbf{s}) = -\frac{1}{2} \sum_{i,j=1, i\neq j}^{N} J(r_{ij})[\mathbf{s}_i \cdot \mathbf{s}_j - 1], \tag{2}$$

where $J(r_{ij})$ is the exchange parameter. Here, we included an offset of the exchange interaction, as detailed in Ma *et al.* [16]. This offset does not affect the precession dynamics of the spins, allowing us instead to offset the corresponding mechanical forces. Without this additional term, the forces and pressure generated by the magnetic Hamiltonian would not be zero at its energy ground state (corresponding to the ferromagnetic state). The spatial dependence of $J(r_{ij})$ is described using the Bethe-Slater curve, as implemented in the SPIN package of LAMMPS [17]

$$J(r_{ij}) = 4\alpha\left(\frac{r_{ij}}{\delta}\right)^2\left[1 - \gamma\left(\frac{r_{ij}}{\delta}\right)^2\right]e^{-\left(\frac{r_{ij}}{\delta}\right)^2}\Theta(R_c - r_{ij}), \tag{3}$$

where $\Theta(R_c - r_{ij})$ is the Heaviside step function and the R_c are the cutoff radii. As shown in previous works [17,18], the dynamics of the coupled spins and atoms can be obtained by integrating the following equations of motion:

$$\begin{aligned} \frac{d\mathbf{r}_i}{dt} &= \frac{\mathbf{p}_i}{m_i}, \\ \frac{d\mathbf{p}_i}{dt} &= -\frac{\partial \mathcal{H}_{sl}}{\partial \mathbf{r}_i}, \\ \frac{d\mathbf{s}_i}{dt} &= \mathbf{w}_i \times \mathbf{s}_i, \end{aligned} \tag{4}$$

where the precession vector

$$\mathbf{w}_i = -\frac{1}{\hbar}\frac{\partial \mathcal{H}_{\text{mag}}}{\partial \mathbf{s}_i} \tag{5}$$

is the analog of a spin force applied to the ith spin. Here, $\hbar$ is the reduced Planck constant.

The effect of temperature is taken into account by connecting thermostats to the corresponding subsystems. Thus, thermal fluctuations in the magnetization are described by the connection of the spin system to a single thermal bath by means of Langevin thermostat that leads to the following stochastic Landau–Lifshitz–Gilbert equation:

$$\frac{d\mathbf{s}_i}{dt} = \frac{1}{1+\lambda^2}((\mathbf{w}_i + \boldsymbol{\eta}(t)) \times \mathbf{s}_i + \lambda \mathbf{s}_i \times (\mathbf{w}_i \times \mathbf{s}_i)), \tag{6}$$

where λ is the transverse damping constant. The properties of such a bath are given by the noise vector $\boldsymbol{\eta}$ whose components follow a Gaussian probability law

$$\begin{aligned} \langle \boldsymbol{\eta}(t) \rangle &= \mathbf{0}, \\ \langle \eta_\alpha(t)\eta_\beta(t') \rangle &= \frac{2\pi\lambda k_B T}{\hbar}\delta_{\alpha\beta}\delta(t - t'), \end{aligned} \tag{7}$$

where α, β are the vector components and the amplitude of the noise is proportional to the given external thermostat T [17,19], and k_B is the Boltzmann constant.

To connect the thermostat to the lattice, we used time integration on Nose-Hoover style non-Hamiltonian equations of motion which are designed to generate positions and velocities sampled from an isothermal-isobaric (*NPT*) ensemble, used in the first thermalization stage, and the canonical (*NVT*) ensemble, used in the dynamics during the pulse application [20,21]. For these thermostats, we set the temperature damping parameter in LAMMPS to 0.01 time steps and the pressure damping parameter to 0.1 time steps, where time step is $dt = 1$ fs.

We point out that in this spin-lattice model, we do not include longitudinal fluctuations of the magnitude of local magnetic moments, so we assume that the ultrafast demagnetization is purely arising from the disordering of spins. Ruban *et al.* [22] studied the temperature-induced longitudinal spin fluctuations in fcc Ni theoretically, finding the average magnitude of magnetic moment changed from $0.6\,\mu_B$ at T = 0 K up to $0.42\,\mu_B$ at 650 K, just above T_C, and to around $0.5\,\mu_B$ at 1300 K. In neutron-diffraction experiment, it was found $0.4\,\mu_B$ measured slightly above T_C [23]. From a theoretical point of view, it is interesting to note that longitudinal spin fluctuations allow us to have an effective finite local magnetic moment at the paramagnetic state in fcc Ni since constrained spin Density Functional Theory predicts a null local magnetic moment [24]. In a classical spin-lattice model without longitudinal spin fluctuations, as our model, a finite local magnetic moment at the paramagnetic state can be achieved by neglecting temperature effects on the magnitude of local magnetic moment. Such approximation has been previously used in atomistic spin dynamics simulations to simulate ultrafast demagnetization in fcc Ni successfully [25]. Longitudinal spin fluctuations can be included in classical spin-lattice models by using the Heisenberg-Landau Hamiltonian [26,27]. Similar simulated ultrafast demagnetization has been obtained in classical spin-lattice models with [27] and without [28] longitudinal spin fluctuations, suggesting a small correction arising from this effect in these models.

B. Spin-lattice model parameters

In our paper, we consider an effective prototype model of fcc Ni. For the classical interatomic potential $\mathcal{V}(r_{ij})$, we use the embedded-atom method potential for fcc Ni developed by Mishin *et al.* [29]. The parameters of the Bethe-Slater curve for $J(r_{ij})$ are calculated to reproduce the desired Curie temperature (T_C) and spontaneous volume magnetostriction (ω_s). Considering exchange interaction up to first-nearest neighbors for a fcc crystal (effective short-range exchange interaction), one finds [30]

$$J(r_0) = \frac{k_B T_C}{4}, \quad r_0 \frac{\partial J}{\partial r}\bigg|_{r=r_0} = \frac{\omega_s(C_{11} + 2C_{12})V_0}{6N}, \tag{8}$$

where C_{11} and C_{12} are the elastic constants, N is the total number of atoms in the equilibrium volume V_0, and r_0 is the equilibrium distance to the first nearest neighbors. The relation between $J(r_0)$ and T_C was obtained using the mean-field approximation. Inserting Eq. (8) into the Bethe-Slater curve and its derivative, and setting $\delta = r_0$ allows us to

TABLE I. Bethe-Slater parameters of the spin-lattice model of fcc Ni and the corresponding value of ω_s.

ω_s	0.001	0.0001	0.00001	−0.00001	−0.0001	−0.001
α(meV)	6.97666	8.95914	9.15738	9.20144	9.39968	11.3822
γ	−0.31573	−0.02459	−0.00241	0.00239	0.02343	0.19353
$\delta = 2.48901$ Å, $R_c = 2.6$ Å						

obtain [31]

$$\alpha = \frac{e}{8}\left[2J(r_0) - r_0 \frac{\partial J}{\partial r}\bigg|_{r=r_0}\right],$$
$$\gamma = \frac{r_0 \frac{\partial J}{\partial r}\big|_{r=r_0}}{r_0 \frac{\partial J}{\partial r}\big|_{r=r_0} - 2J(r_0)}, \tag{9}$$

where e is Euler's number and the exchange cutoff radius R_c must be in between the first and second nearest neighbors ($R_c = 2.6$ Å). The equilibrium interatomic distance between first-nearest neighbors is obtained by fitting the energy-volume curve to the Murnaghan equation of state [32,33]. This procedure yields $r_0 = 2.48901$ Å, so the lattice parameter is $a = \sqrt{2}r_0 = 3.51999$ Å. The magnetic moment is $\mu = 0.61\,\mu_B$ [34] and the mass is 58.69 g/mole. The elastic constants are evaluated through the energy-strain method at zero temperature, as implemented in AELAS [35], finding $C_{11} = 259$ GPa, $C_{12} = 156$ GPa, and $C_{44} = 131$ GPa, and thus agreeing with available experimental data from Ref. [36]: $C_{11} = 261.2$ GPa, $C_{12} = 150.8$ GPa, $C_{44} = 131.7$ GPa (at $T = 0$ K) and $C_{11} = 250.8$ GPa, $C_{12} = 150.0$ GPa, $C_{44} = 123.5$ GPa (at $T = 300$ K). The Curie temperature is set to the experimental value $T_C = 627$ K [34]. It is interesting to study the relationship between ω_s (the exchange isotropic magnetostriction) and the elastic wave generated by an ultrafast demagnetization. To do so, we consider a set of ω_s values in the model ($\omega_s = \pm 0.001, \pm 0.0001, \pm 0.00001$). The other reason to use such a set of values is the fact that the exact value of the spontaneous volume magnetostriction for fcc Ni [37] is still an open question and different values can be found in different publications: $\sim 10^{-3}$ [38], $\sim 10^{-4}$ [39,40] and negative values have also been reported [41,42]. The values of the Bethe-Slater parameters for $J(r)$ that lead to the desired ω_s in the model are found by combining Eqs. (8) and (9); see Table I. Extensions of this model that include magnetocrystalline anisotropy and anisotropic magnetostriction can be achieved by using the Néel model [31]. In Appendix A, we verify that the anisotropic effects do not significantly change the results found using the isotropic model. The value of transverse damping constant λ for fcc Ni was set to $\lambda(T) = \Theta/T$, where $\Theta = 3$ K, similar to Ref. [43].

The atomic magnetic moments in this spin-lattice model are considered effective localized moments at the lattice sites, but Ni is a metal and the magnetism here is rather described by the itinerant (delocalized, conduction band) electrons. The amount of electron localization has long been debated in 3d metals, as the magnetism comes from the outer electrons that are considered to be loosely bound to the atoms. First-principles calculations of the electron density [44] indicate that, in practice, even in itinerant ferromagnets, the spin polarization is concentrated at the atomic sites. This means that the bonding electrons are not polarized, and once the bonding charge is accounted for, the remaining d electrons create a clearly defined effective localized moment at the atomic sites [45].

C. Computational details

As a simple model for atomistic spin-lattice simulations in LAMMPS [17], we take a box of size $352 \times 35.2 \times 35.2$ Å^3 and periodic boundary conditions. The box consists of two regions of identical Ni atoms (with a total of 40 000 atoms in the box) ferromagnetically ordered along the **z** direction and initially thermalized at a temperature $T = 300$ K (Fig. 1). Note this model is isotropic but for real fcc Ni, the hard and easy axis are, respectively, [100] and [111]. Magnetic anisotropy effects are examined in Appendix A. After that, in region 1 of size $35.2 \times 35.2 \times 35.2$ Å^3, we begin to increase the temperature as a surrogate of the heating from a laser.

To realistically describe the effect of a femtosecond laser pulse on region 1, we include thermostats in Eqs. (4) [17]. We assume that the pulse is absorbed by electrons and the magnetic system is coupled to the electron bath, so the temperature of the spin system corresponds to the electron bath temperature. To reach a quantitative agreement of the temperature-dependent magnetization between simulation and experiments according to Evans *et al.* [25], we then rescale the spin bath temperature for Ni as

$$\frac{T_{\text{sim}}}{T_C} = \left(\frac{T_{\text{exp}}}{T_C}\right)^{2.322}. \tag{10}$$

The electron bath temperature is obtained from the numerical integration of the two-temperature model (2TM) [46,47]

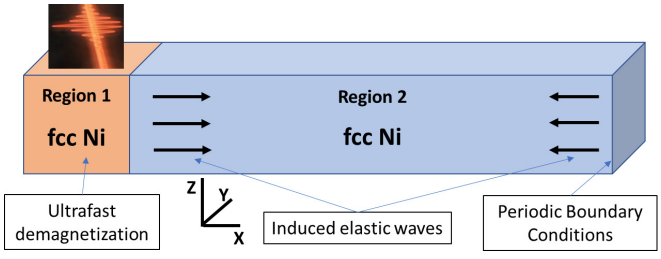

FIG. 1. Diagram showing the model configuration to simulate the elastic waves induced by ultrafast demagnetization. The crystallographic directions [100], [010], [001] coincide with the axes **x**, **y**, **z**, respectively.

given by

$$C_e\frac{dT_e}{dt} = -g_{ep}(T_e - T_{\rm ph}) + P(t),$$
$$C_{\rm ph}\frac{dT_{\rm ph}}{dt} = g_{ep}(T_e - T_{ph}), \tag{11}$$

where T_e is the electronic temperature, $T_{\rm ph}$ is the lattice or phonon temperature, $C_e(T_e) = \gamma_e T_e$, $\gamma_e = 3000$ J/m^{3}K^2 [46], and $C_{\rm ph} = 2.2 \times 10^6$ J/m^{3}K [10] are the specific heats of the electrons and lattice, $g_{ep} = 1.2 \times 10^{18}$ J/s m^{3}K [25] is an electron-phonon coupling constant which determines the rate of the energy exchange between the electrons and the lattice, and P is the deposited laser energy. To model the optical pulse excitation in the 2TM, we use the expression from Shalaby *et al.* [48],

$$P(t) = \frac{AF}{\sqrt{2\pi}\tau d}e^{\frac{-t^2}{2\tau^2}}, \tag{12}$$

where $A = 0.11$ is the absorption coefficient, $F = 10$ mJ/cm^2 is the incident fluence, $d = 15$ nm is the film thickness, and $\tau = 60$ fs is the temporal width of the pulse.

The temperature in the equation of motion of spins [Eqs. (6) and (7)] corresponds to T_e, while for the lattice thermostat is $T_{\rm ph}$. In this way, we have a model for ferromagnetically ordered fcc Ni that reproduces the absorption of some optical energy from the laser pulse by the surface and its transformation into lattice expansion, as well as demagnetization, which in turn affects the lattice expansion due to magnetostriction effects. In our model, there is actually an energy transfer from an electron to spin subsystem since the bath temperature of spins in Eq. (6) corresponds to the electronic temperature (T_e) but, for the sake of simplicity, we neglected the energy transfer from a spin to electron subsystem. Such energy transfer can be included by adding a term in the differential equation of T_e in the 2TM [Eq. (11)] associated to the spin dynamics of the form $\sum_i \mathbf{H}_i^{\rm eff}\cdot(d\boldsymbol{\mu}_i/dt)$, where $\boldsymbol{\mu}_i = \mu\mathbf{s}_i$ is the atomic magnetic moment vector, $\mathbf{H}_i^{\rm eff} = -\partial\mathcal{H}_{\rm mag}/\partial\boldsymbol{\mu}_i$ is the effective field, and index i in the summation runs over all spins in the system [49,50]. According to our numerical tests, this additional term gives a small correction to the overall dynamics which does not significantly change the presented results. The energy transfer between spins and lattice is achieved through the spatial dependence of exchange interaction, as well as via the Néel model in the case with anisotropy discussed in Appendix A. Recently, heat conservation in spin-lattice simulations of ultrafast demagnetization has been studied by Pankratova *et al.* [51,52].

III. THEORY OF THE STRAIN RESPONSE

The governing equation of picosecond ultrasound dynamics may be written as [1]

$$\rho\frac{\partial^2 u_x}{\partial t^2} = \frac{\partial}{\partial x}\left(C_{11}\epsilon_{xx} + \sigma_{xx}^{\rm ext}\right) = C_{11}\frac{\partial^2 u_x}{\partial x^2} + \frac{\partial\sigma_{xx}^{\rm ext}}{\partial x}. \tag{13}$$

Equation (13) is the elastic wave equation, i.e., the equation of motion for the displacement component $u_x(x,t)$, where ρ is the mass density and the deformation of the solid is described by the strain $\epsilon_{xx} = \partial u_x/\partial x$. Here, for convenience, we use the positive sign for the external stress $\sigma_{xx}^{\rm ext}$ so a negative longitudinal stress that acts from within the material leads to an expansion along the direction of the stress. Note that this is the opposite convention as in Mattern *et al.* [1]. The total external stress may be written according to Refs. [1,3] as

$$\sigma_{xx}^{\rm ext,total}(T) = -C_{11}\alpha^{\rm uf}(T - T_0), \tag{14}$$

where T is the temperature compared to the reference temperature T_0 before the arrival of the optical pulse.

The ultrafast expansion coefficient for a metal with typical Poisson constant $\nu \approx 1/3$ is approximately twice larger than the equilibrium thermal expansion coefficient $\alpha^{\rm uf} = \alpha^{\rm eq}(1 + 2C_{12}/C_{11}) \approx 2\alpha^{\rm eq}$ [1].

In Appendix B, we find that the magnetic contribution to the external stress is approximately

$$\sigma_{xx}^{\rm ext,mag} \approx (C_{11} + 2C_{12})\frac{\omega_s}{3}(m_0 - m) \tag{15}$$

in terms of the normalized magnetization $m = |\mathbf{m}| = M/M_s(T = 0K)$ at time t, where m_0 is the normalized magnetization before the laser action, and ω_s is the spontaneous volume magnetostriction just as in the spin-lattice model.

IV. RESULTS

A. Waves generated by ultrafast magnetic disordering

First, we decided to single out the effect arising from ultrafast demagnetization (which in this subsection is rudely simplified to ultrafast magnetic disordering without heat effects). For this purpose, we used atomistic spin-lattice simulations and set a constant temperature of 0 K and the corresponding equilibrium lattice parameter for the ferromagnetic state in the entire sample to avoid thermal effects. At the initial time, in region 1 we set a random orientation for the spins, while in region 2 the spins are oriented parallel to the **z** axis. We found that such a rapid change in the orientation of the spins to a random one causes an elastic wave in the adjacent magnetically ordered region 2 due to exchange magnetostriction (ω_s), which propagates with a velocity $v = 5280$ m/s and thus practically corresponds to the speed of sound of a longitudinal wave along the crystallographic direction [100] in Ni $v_{\rm sound} = \sqrt{C_{11}/\rho} = 5379.39$ m/s (shown in Fig. 2). The amplitude of such a wave is proportional to ω_s, as seen in Fig. 2(b), and depends on the width in the **x** direction of the magnetically disordered region. To investigate the effect of the size of region 1 on the resulting properties of the elastic wave, we increased the sample size in the model up to $880 \times 35.2 \times 35.2$ Å^3 and approximated the elastic wave by a Gaussian function,

$$u_x(x,t) = a_m e^{-(x - v(t - t_m))^2/2\sigma^2}, \tag{16}$$

where $u_x(x,t)$ is the average displacement (in the **x** direction) of atoms located on the crystallographic plane with the x coordinate at time t, a_m is the wave amplitude, v is the speed of the wave, t_m is the fitting parameter which in our model is taken equal to 100 fs, and σ is the Gaussian width parameter which is responsible for the full width half maximum (FWHM) of the resulting elastic wave as FWHM $= \sigma\sqrt{8\ln 2}$.

Thus, this effect is relatively small in comparison to the thermal expansion and is mainly of purely theoretical interest, while for the interpretation of the results from experimental

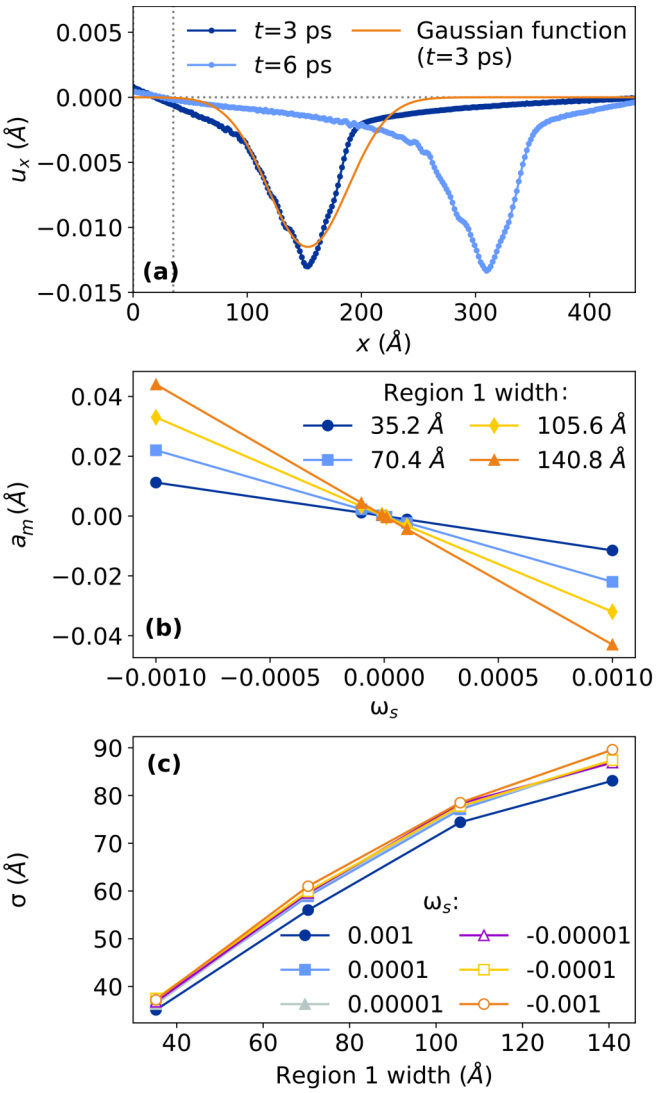

FIG. 2. The elastic wave induced by the magnetic disorder in region 1. (a) Elastic wave propagation and approximation of the wave by a Gaussian function. As an example, the wave profile in two time moments for the case of $\omega_s = 0.001$ is shown. The vertical dotted line shows the boundary between region 1 and region 2. (b) Dependence of the elastic wave amplitude a_m on the volume magnetostriction ω_s and the size of region 1. (c) Gaussian width parameter σ dependence on the width of the magnetically disordered region.

studies, it is necessary to take into account the effects associated with heating.

B. Waves generated by ultrafast heating

In this section, we consider the spin-lattice model with $\omega_s = 0.001$ to study heat effects. As follows from a comparison with experimental data [10] in Fig. 3(a), the temperature model we have proposed in Sec. II C describes the laser-induced temperature change in region 1 quite well, and this leads to a correct representation of the demagnetization processes in our atomistic spin-lattice simulations as shown in Fig. 3(b). We also see our approach leads to similar overall dynamics as the three temperature model (3TM) used by Beaurepaire *et al.* [10]. For example, remarkable similarities

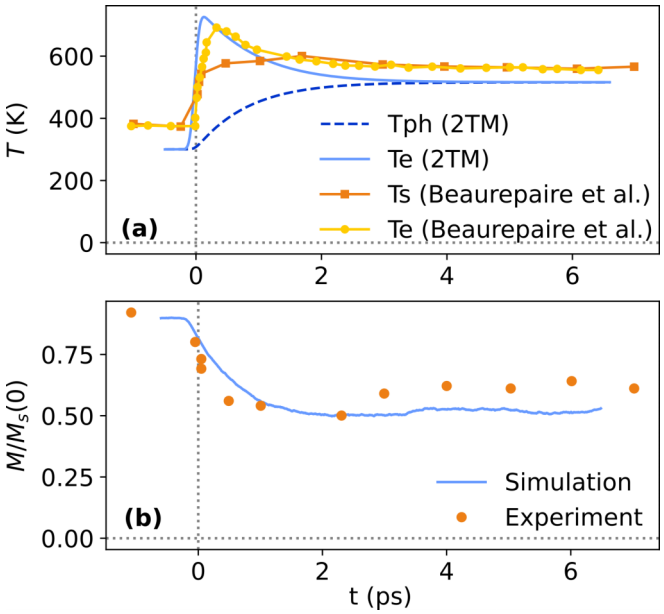

FIG. 3. (a) Temporal evolution of different contributions to the temperature in region 1 in our simulations (according to 2TM), namely, phononic (blue dashed line), electronic (light blue line) and, following Beaurepaire [10], spin (orange) and electronic (yellow) using the 3TM. (b) Subpicosecond demagnetization (normalized) in region 1 induced by femtosecond laser pulse: our model (blue) versus experimental data (orange symbols) from Beaurepaire *et al.* [10].

between the microscopic implementation of the 3TM (so-called M3TM) [53] and coupling magnetic dynamics to the 2TM has been reported [54]. Rapid heating and the resulting demagnetization create stress in region 1, the averaged component σ_{xx}^{ext} of which is shown in Fig. 4. This stress can be successfully approximated [as can be seen on Fig. 4(a)] by an exponential function as

$$\sigma_{xx}^{\text{ext,total}}(t) = a_0 e^{-bt} - c_0 = a_0(e^{-bt} - e^{-bt_0}), \tag{17}$$

where a_0, b, and $c_0 = a_0 e^{-bt_0}$ are fitting parameters.

To evaluate the magnetic contribution to the total stress, we performed an additional simulation that shows the contribution of the lattice alone without spin interactions (silver line in Fig. 4). From the total stress, we define the contribution responsible for the magnetic subsystem as $\sigma_{xx}^{\text{ext,mag}} = \sigma_{xx}^{\text{ext,total}} - \sigma_{xx}^{\text{ext,lat}}$ and compare it with the theoretical, Eq. (15). As can be seen from Fig. 4(a), although the $\sigma_{xx}^{\text{ext,mag}}$ obtained from simulations has certain inaccuracies, on average it agrees quite well with the theoretical expression (15). In the simulation for $\sigma_{xx}^{\text{ext,total}}$ and in the formula for $\sigma_{xx}^{\text{ext,mag}}$, we have supposed $\omega_s = 0.001$ according to the used spin-lattice model.

Additionally, we compared our simulation results for the total external stress with the temperature dependence represented by Eq. (14) and find good agreement (linear dependence) only for phonon temperature case,

$$\sigma_{xx}^{\text{ext,total}}(T_{\text{ph}}) = -C_{11}\alpha^{\text{uf}}(T_{\text{ph}} - T_{\text{ph0}}), \tag{18}$$

while Eq. (14) is written with the assumption that the temperatures of the different degrees of freedom are the same and therefore does not contain the specification of this temperature. The value $\alpha^{\text{uf}} = 2.671 \times 10^{-5}$ K^{-1} obtained from the

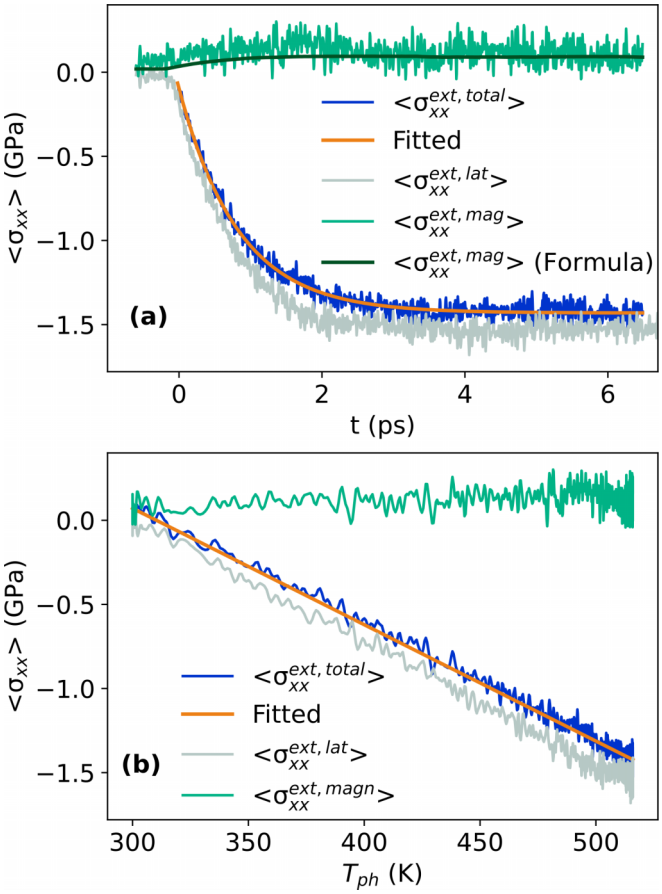

FIG. 4. (a) Time dependence of total stress (blue line), magnetic contribution to external stress (green line), and lattice contribution to external stress (silver line). Orange line shows the approximation to the total stress by using formula (17) with fitting parameters $a_0 = 1.334$ GPa, $b = 1.206$ ps^{-1}, and $t_0 = -0.058$ ps (or $c_0 = -1.431$ GPa). The dark green line is the theoretical magnetic contribution to the external stress from Eq. (15). (b) Lattice temperature dependence of average stresses in region 1. The orange line shows the approximation to the total stress by using formula (14) with fitting parameter $\alpha^{\text{uf}} = 2.671 \times 10^{-5}$ K^{-1}.

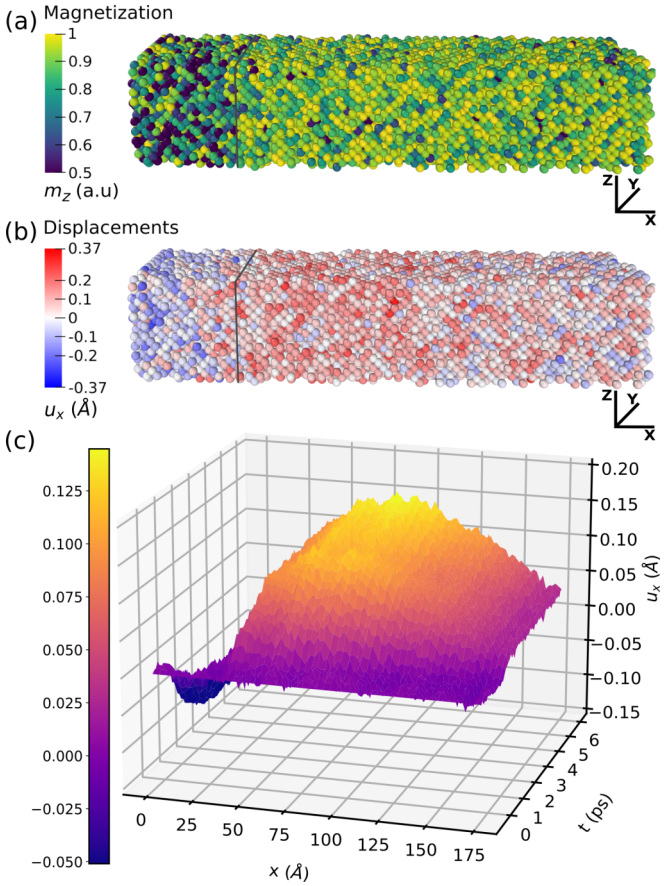

FIG. 5. The heating-induced demagnetization as simulated in LAMMPS and the corresponding atomic displacements. (a) Spatial distribution of the magnetization component along the **z** direction $m_z(x)$ at time $t = 1.65$ ps. The heated region is clearly visible due to noticeable demagnetization. (b) The atomic displacements along **x** direction $u_x(x)$ in Å at the same time. (c) Displacement component $u_x(x, t)$ as averaged in crystallographic planes, where the coordinate x corresponds to the coordinate of the crystallographic plane. All data in (a)–(c) are shown for the coordinate x ranging from 0 to 176 Å, which includes the heated region (region 1) and approximately half the adjacent region (region 2).

approximation in Fig. 4(b) is indeed about twice times larger than the calculated equilibrium thermal expansion coefficient $\alpha^{\text{eq}} = 1.192 \times 10^{-5}$ K^{-1} (including the magnetic part, i.e., ω_s).

It is noteworthy that the external stress in Eq. (17) and Eq. (18) is the same stress expressed in terms of time or lattice temperature, which can be written as average values for region 1 in the same way as the exact values for some point with coordinate x_i [with stress amplitude $a_0(x_i)$ correction with respect to coordinate x_i] in region 2. This gives us the opportunity to obtain the time dependence of the phonon temperature expressed in terms of external stress parameters as

$$T_{\text{ph}}(t) = T_{\text{ph0}} + \frac{a_0}{C_{11}\alpha^{\text{uf}}}(e^{-bt} - e^{-bt_0}), \tag{19}$$

which might be useful for temperature T_{ph} analysis in picosecond ultrasonics experiments. Nevertheless, in this case, further analysis of the physical nature of the fitting parameters a_0 and b is required.

To study the elastic response in region 2 to laser-induced heating in region 1, it is necessary to take into account the spatial dependence of the studied physical quantities. While a purely analytical consideration of the solution of the equation of motion Eq. (13) requires knowledge of the explicit dependence of the stress $\sigma_{xx}^{\text{ext,total}}(x, t)$ on both time and coordinate x (that are not currently known), in atomistic simulations there is no such problem. Thus, the effect of heating on the magnetic subsystem (the component of magnetization along the **z** direction) obtained from the simulation in LAMMPS and visualized in OVITO [55] at time $t = 1.65$ ps is shown in Fig. 5(a), while the state of the elastic subsystem (displacements along the **x** direction) at this same time are represented in Fig. 5(b). Further analysis of the simulation data allows us to depict a map of the spatial-time dependence of displacements averaged in the crystallographic planes.

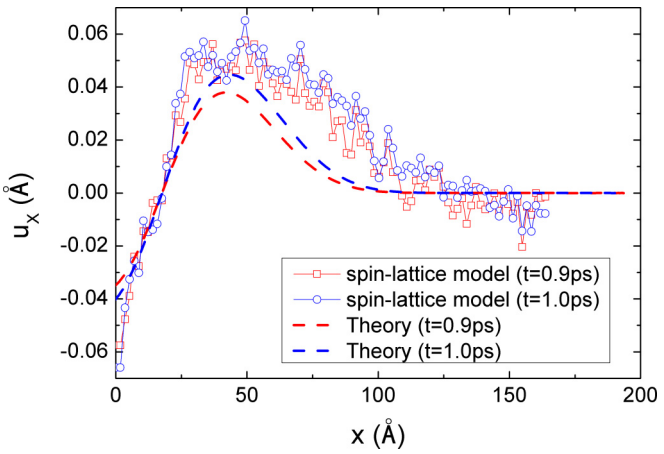

FIG. 6. LAMMPS simulation vs numerical solution of the governing equation of picosecond ultrasonics, Eq. (13), with the total external stress as specified in Eq. (20).

From the spatial and time dependencies of displacements $u_x(x,t)$, it is possible to make an assumption about the specified time and coordinate dependent parts of the analytical expression of the external stresses. The total external stress shows a tendency for exponential dependencies on time in the entire sample and not only in the heated region 1, but the specific value of stress at a certain point depends on coordinate x. Therefore, the spatial dependence of the $\sigma_{xx}^{\text{ext,total}}$ can be found by correction to its amplitude as $a_0(x) = a_0^{\text{const}} f(x)$ in Eq. (17), where the explicit analytical expression of the function $f(x)$ is unknown. To reach an agreement with the $u_x(x,t)$ obtained in the simulation, we propose to express this function in the form $f(x) = e^{-\frac{1}{2}(\frac{x-x_0}{\Delta x})^2}$, where $\Delta x = 17.6$ Å is half the size of region 1 and $x_0 = 17.6$ Å is the coordinate of the center of the heated region. For simplicity, in the following example, we take approximately $a_0^{\text{const}} \approx a_0 = 1.334$ GPa found in Fig. 4 (although the average value of the amplitude in region 1 can formally be obtained by integration as $\frac{a_0^{\text{const}}}{2\Delta x}\int_0^{2\Delta x} e^{-\frac{1}{2}(\frac{x-x_0}{\Delta x})^2}\,dx$ giving a scaling factor between these two quantities).

The total stress specified as

$$\sigma_{xx}^{\text{ext,total}}(x,t) = a_0^{\text{const}}(e^{-bt} - e^{-bt_0})e^{-\frac{1}{2}(\frac{x-x_0}{\Delta x})^2} \tag{20}$$

can then be substituted directly into the governing equation of picosecond ultrasound dynamics, Eq. (13), and the solution of the latter by numerical methods shows quite good agreement with atomistic simulation data, as can be seen from Fig. 6.

In summary, we have proposed a theoretical model for simulating laser-induced responses of the elastic and magnetic subsystems of the crystal, clarified the type of temperature in Eq. (14), clarified the magnetic contribution to the total stress, and proposed an analytical expression for the total stress. The presented results, including analytical expressions, can be experimentally verified in picosecond ultrasonics experiments using ultrashort hard x-ray pulses.

V. CONCLUSIONS

We have proposed a method of using the SPIN package of LAMMPS to simulate the laser-induced elastic response in picosecond ultrasonics. The advantages of the proposed method are the possibility of creating more realistic 3D models of crystal structures that are able to take into account the defects, system geometry, crystal orientation, the magnetic ordering, and the possibility of obtaining complete strain and stress tensors. Based on the example of fcc Ni, we have shown how this method can be applied to ferromagnetically ordered materials and have characterized the magnetic contribution to the stress. The ferromagnetically ordered Ni example considered in the present paper shows good agreement of the simulation results with both available experimental data and previous theoretical models.

The theoretical approach presented in our paper can be useful for further interpretations of experiments in the picosecond ultrasonics, as well as for providing other required parameters (like ultrafast thermal expansion coefficient α^{uf}) in micromagnetic models of picosecond ultrasonics within a multiscale approach.

As a possible further development of the proposed model, we suggest trying to apply a similar approach to the description and investigation of phenomena related to demagnetization due to x-ray [56–61], where the ultrafast demagnetization and related processes proceed even faster.

ACKNOWLEDGMENTS

This work was supported by Projects e-INFRA CZ (ID No. 90254) and QM4ST (No. CZ.02.01.01/00/22_008/0004572) by the Ministry of Education, Youth and Sports of the Czech Republic, and also by Czech Science Foundation of the Czech Republic by Grant No. 22-35410K. P.N. acknowledges support by Grant No. MU-23-BG22/00168 funded by the Ministry of Universities of Spain. A.F. acknowledges funding from the Spanish Ministry of Science and Innovation (Grants No. PID2022-139230NB-I00 and No. TED2021-132074B-C32) the Diputación Foral de Gipuzkoa (Project No. 2023-CIEN-000077-01). Research was conducted in the scope of the Transnational Common Laboratory (LTC) Aquitaine-Euskadi Network in Green Concrete and Cement-based Materials. R.I. acknowledges financial support from the project MAGNES funded by the Principality of Asturias Government (Grant No. AYUD/2021/51822) and from the project RADIAFUS V, funded by the Spanish Ministry of Science and Innovation (Grant No. PID2019-105325RB-C32).

APPENDIX A: MAGNETIC ANISOTROPIC EFFECTS

The magnetic anisotropic effects can be included in the spin-lattice model by adding the Néel interaction in the magnetic energy [Eq. (2)] [30,31] through a two-ion Hamiltonian [62]

$$\begin{aligned}\mathcal{H}_{\text{Néel}} = -\frac{1}{2}\sum_{i,j=1}^{N}\{&l_1(r_{ij})\left[(\boldsymbol{e}_{ij}\cdot\boldsymbol{s}_i)(\boldsymbol{e}_{ij}\cdot\boldsymbol{s}_j) - \frac{\boldsymbol{s}_i\cdot\boldsymbol{s}_j}{3}\right]\\ &+ q_1(r_{ij})\left[(\boldsymbol{e}_{ij}\cdot\boldsymbol{s}_i)^2 - \frac{\boldsymbol{s}_i\cdot\boldsymbol{s}_j}{3}\right]\left[(\boldsymbol{e}_{ij}\cdot\boldsymbol{s}_j)^2 - \frac{\boldsymbol{s}_i\cdot\boldsymbol{s}_j}{3}\right]\\ &+ q_2(r_{ij})[(\boldsymbol{e}_{ij}\cdot\boldsymbol{s}_i)(\boldsymbol{e}_{ij}\cdot\boldsymbol{s}_j)^3 + (\boldsymbol{e}_{ij}\cdot\boldsymbol{s}_j)(\boldsymbol{e}_{ij}\cdot\boldsymbol{s}_i)^3]\},\end{aligned} \tag{A1}$$

where $\boldsymbol{e}_{ij} = \boldsymbol{r}_{ij}/r_{ij}$ and

$$\begin{aligned} l_1(r_{ij}) &= l(r_{ij}) + \tfrac{12}{35} q(r_{ij}), \\ q_1(r_{ij}) &= \tfrac{9}{5} q(r_{ij}), \\ q_2(r_{ij}) &= -\tfrac{2}{5} q(r_{ij}). \end{aligned} \tag{A2}$$

The dipole $[l(r_{ij})]$ and quadrupole $[q(r_{ij})]$ terms can describe the anisotropic effects induced by spin-orbit coupling like the anisotropic magnetostriction (λ_{100} and λ_{111}) and magnetocrystalline anisotropy (K_1), respectively [30,31]. As for the exchange parameter $J(r_{ij})$, we describe the spatial dependence of $l(r_{ij})$ and $q(r_{ij})$ using the Bethe-Slater curve, as implemented in the SPIN package of LAMMPS [17]:

$$\begin{aligned} l(r_{ij}) &= 4\alpha_l \left(\frac{r_{ij}}{\delta_l}\right)^2 \left[1 - \gamma_l \left(\frac{r_{ij}}{\delta_l}\right)^2\right] e^{-\left(\frac{r_{ij}}{\delta_l}\right)^2} \Theta(R_{c,l} - r_{ij}), \\ q(r_{ij}) &= 4\alpha_q \left(\frac{r_{ij}}{\delta_q}\right)^2 \left[1 - \gamma_q \left(\frac{r_{ij}}{\delta_q}\right)^2\right] e^{-\left(\frac{r_{ij}}{\delta_q}\right)^2} \Theta(R_{c,q} - r_{ij}). \end{aligned} \tag{A3}$$

For fcc Ni, we use the following values of these parameters: $\alpha_l = 179.396$ μeV/atom, $\gamma_l = 1.39848$, $\delta_l = 2.48901$ Å, $R_{c,l} = 2.6$ Å, $\alpha_q = -49.1335$ μeV/atom, $\gamma_q = 1.1186$, $\delta_q = 2.48901$ Å, and $R_{c,q} = 2.6$ Å, which were previously found to reproduce experimental anisotropic magnetostriction (λ_{100} and λ_{111}) and magnetocrystalline anisotropy at zero temperature (K_1) [31].

In the case of fcc Ni, taking into account the effects of magnetic anisotropy in the study of ultrafast heat-induced demagnetization does not lead to noticeable effects, as can be seen from Fig. 7. The obtained difference in the averaged stress σ_{xx} in the heated region is relatively small and can be explained both by the effects of anisotropy and the limited accuracy of the measurement of this value in the proposed model. We think this result is consistent with theory since magnetic stress is proportional to spontaneous volume magnetostriction ω_s [see (B9)], and ω_s only depends on isotropic magnetostrictive coefficient (λ^α) up to first order in cubic crystals $\omega_s = 3\lambda^\alpha + O(\lambda_{100}^2, \lambda_{111}^2)$ [37]. Hence, according to this argument, one might expect very small anisotropic effects on magnetic stress during ultrafast demagnetization in cubic crystals like fcc Ni. Conservation of angular momentum of this spin-lattice model has been recently studied by Cooke and Lukes [63]. Note that more advanced models like *ab initio* nonadiabatic molecular dynamics may be required to describe spin-orbit coupling effects on the electronic structure during ultrafast demagnetization [64].

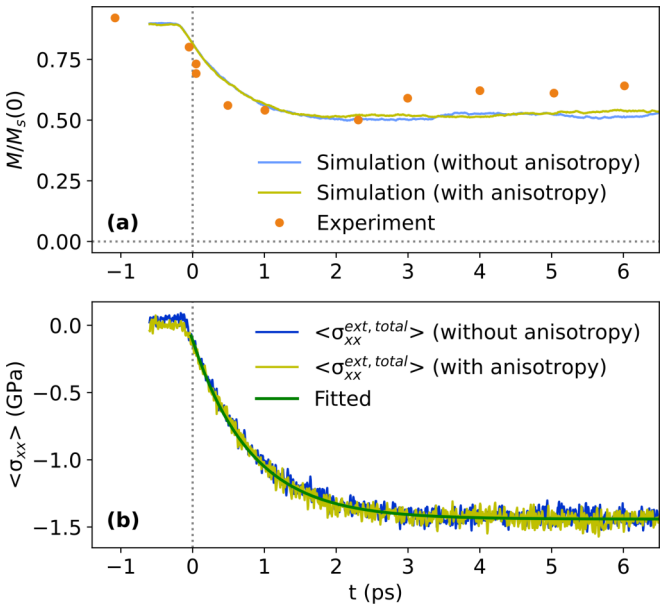

FIG. 7. Magnetic anisotropic effects. (a) Demagnetization in region 1 induced by femtosecond laser pulse: model with neglected (blue) and model with included magnetic anisotropy effects (yellow) versus experiment (orange symbols) from Beaurepaire *et al.* [10]. In the model with anisotropy, the direction of the initial magnetization is set along the easy crystallographic axis [111]. (b) Changes in the total stress with respect to including the effects of magnetic anisotropy. Green line shows the approximation of the total stress (with magnetic anisotropy effects) by Eq. (17) with fitting parameters $a_0 = 1.329$ GPa, $b = 1.227$ ps^{-1}, and $t_0 = -0.066$ ps (or $c_0 = -1.441$ GPa).

APPENDIX B: MAGNETIC STRESS

In this Appendix, we derive some theoretical expressions for the magnetic contribution to stress. The stress tensor σ_{ij} is related to the fourth-order elastic stiffness tensor c_{ijkl} and the second-order strain tensor ϵ_{ij} through the generalized Hooke's law:

$$\sigma_{ij} = \sum_{k,l=x,y,z} c_{ijkl}\epsilon_{kl}, \quad i, j = x, y, z. \tag{B1}$$

Using the symmetry of the stress and strain tensors, Hooke's law can be written in matrix notation as

$$\begin{pmatrix} \sigma_{xx} \\ \sigma_{yy} \\ \sigma_{zz} \\ \sigma_{yz} \\ \sigma_{zx} \\ \sigma_{xy} \end{pmatrix} = \begin{pmatrix} c_{xxxx} & c_{xxyy} & c_{xxzz} & c_{xxyz} & c_{xxzx} & c_{xxxy} \\ c_{yyxx} & c_{yyyy} & c_{yyzz} & c_{yyyz} & c_{yyzx} & c_{yyxy} \\ c_{zzxx} & c_{zzyy} & c_{zzzz} & c_{zzyz} & c_{zzzx} & c_{zzxy} \\ c_{yzxx} & c_{yzyy} & c_{yzzz} & c_{yzyz} & c_{yzzx} & c_{yzxy} \\ c_{zxxx} & c_{zxyy} & c_{zxzz} & c_{zxyz} & c_{zxzx} & c_{zxxy} \\ c_{xyxx} & c_{xyyy} & c_{xyzz} & c_{xyyz} & c_{xyzx} & c_{xyxy} \end{pmatrix} \times \begin{pmatrix} \epsilon_{xx} \\ \epsilon_{yy} \\ \epsilon_{zz} \\ 2\epsilon_{yz} \\ 2\epsilon_{zx} \\ 2\epsilon_{xy} \end{pmatrix}. \tag{B2}$$

To facilitate the manipulation of this equation, it is convenient to define the following six-dimensional vectors (Voigt notation):

$$\tilde{\boldsymbol{\sigma}} = \begin{pmatrix} \tilde{\sigma}_1 \\ \tilde{\sigma}_2 \\ \tilde{\sigma}_3 \\ \tilde{\sigma}_4 \\ \tilde{\sigma}_5 \\ \tilde{\sigma}_6 \end{pmatrix} = \begin{pmatrix} \sigma_{xx} \\ \sigma_{yy} \\ \sigma_{zz} \\ \sigma_{yz} \\ \sigma_{zx} \\ \sigma_{xy} \end{pmatrix}, \qquad \tilde{\boldsymbol{\epsilon}} = \begin{pmatrix} \tilde{\epsilon}_1 \\ \tilde{\epsilon}_2 \\ \tilde{\epsilon}_3 \\ \tilde{\epsilon}_4 \\ \tilde{\epsilon}_5 \\ \tilde{\epsilon}_6 \end{pmatrix} = \begin{pmatrix} \epsilon_{xx} \\ \epsilon_{yy} \\ \epsilon_{zz} \\ 2\epsilon_{yz} \\ 2\epsilon_{zx} \\ 2\epsilon_{xy} \end{pmatrix}, \tag{B3}$$

and replace c_{ijkl} by C_{nm} contracting a pair of Cartesian indices into a single integer: $xx \to 1$, $yy \to 2$, $zz \to 3$, $yz \to 4$, $zx \to 5$, and $xy \to 6$. Using these conversion rules, Hooke's law is simplified to

$$\tilde{\sigma}_i = \sum_{j=1}^{6} C_{ij}\tilde{\epsilon}_j, \quad i = 1, ..., 6, \tag{B4}$$

which in matrix form reads

$$\begin{pmatrix} \tilde{\sigma}_1 \\ \tilde{\sigma}_2 \\ \tilde{\sigma}_3 \\ \tilde{\sigma}_4 \\ \tilde{\sigma}_5 \\ \tilde{\sigma}_6 \end{pmatrix} = \begin{pmatrix} C_{11} & C_{12} & C_{13} & C_{14} & C_{15} & C_{16} \\ C_{21} & C_{22} & C_{23} & C_{24} & C_{25} & C_{26} \\ C_{31} & C_{32} & C_{33} & C_{34} & C_{35} & C_{36} \\ C_{41} & C_{42} & C_{43} & C_{44} & C_{45} & C_{46} \\ C_{51} & C_{52} & C_{53} & C_{54} & C_{55} & C_{56} \\ C_{61} & C_{62} & C_{63} & C_{64} & C_{65} & C_{66} \end{pmatrix} \begin{pmatrix} \tilde{\epsilon}_1 \\ \tilde{\epsilon}_2 \\ \tilde{\epsilon}_3 \\ \tilde{\epsilon}_4 \\ \tilde{\epsilon}_5 \\ \tilde{\epsilon}_6 \end{pmatrix}. \tag{B5}$$

Hence, for cubic crystals the xx component of stress is simplified to

$$\tilde{\sigma}_1 = \sigma_{xx} = C_{11}\epsilon_{xx} + C_{12}(\epsilon_{yy} + \epsilon_{zz}). \tag{B6}$$

Now, let us assume that the system is initially at the equilibrium ferromagnetic state at zero temperature ($m_0 = 1$, $V = V_{\mathrm{FM}}$ and $T_0 = 0$ K), and we suddenly set the spins to a paramagnetic state ($m = 0$) but with frozen lattice ($V = V_{\mathrm{FM}}$). In this case, the trace of the induced strain tensor is equal to the spontaneous volume magnetostriction:

$$\omega_s = \frac{V_{\mathrm{FM}} - V_{\mathrm{PM}}}{V_{\mathrm{PM}}} \simeq \epsilon_{xx} + \epsilon_{yy} + \epsilon_{zz}. \tag{B7}$$

Since we also have $\epsilon_{xx} = \epsilon_{yy} = \epsilon_{zz}$, then

$$\epsilon_{xx} = \epsilon_{yy} = \epsilon_{zz} = \frac{\omega_s}{3}. \tag{B8}$$

Inserting Eq. (B8) in Eq. (B6) leads to

$$\sigma_{xx}^{\mathrm{mag}} = (C_{11}(T_0) + 2C_{12}(T_0))\frac{\omega_s(T_0)}{3}. \tag{B9}$$

This relationship can be also obtained from bulk modulus $B_0 = -V(dP/dV)$ since for cubic crystals $B_0 = (C_{11} + 2C_{12})/3$.

For our model of fcc Ni with $\omega_s = 0.001$ (where $C_{11} = 259$ GPa and $C_{12} = 156$ GPa), the theoretical induced magnetic stress is $\sigma_{xx}^{\mathrm{mag}} = 0.1905$ GPa from Eq. (B9), finding good agreement with the spin-lattice model simulation (0.1903 GPa). In Fig. 8, we numerically verified with spin-lattice simulations that for an arbitrary demagnetized state m the magnetic stress follows approximately

$$\sigma_{xx}^{\mathrm{mag}}(m) \approx (C_{11}(T_0) + 2C_{12}(T_0))\frac{\omega_s(T_0)}{3}(1 - m), \tag{B10}$$

where Eq. (B9) is recovered for the fully demagnetized state $m = 0$. Thus, the change in magnetic stress between two arbitrary magnetic states m_1 and m_2 may be written as

$$\delta\sigma_{xx}^{\mathrm{mag}} = \sigma_{xx}^{\mathrm{mag}}(m_2) - \sigma_{xx}^{\mathrm{mag}}(m_1) \approx (C_{11} + 2C_{12})\frac{\omega_s}{3}(m_1 - m_2). \tag{B11}$$

We see that an ultrafast change in magnetization $\delta m = m_1 - m_2$ induces a change in the magnetic contribution to stress due to exchange magnetostriction ω_s, as shown in Fig. 4. Note also that the sign of this stress depends on the sign of ω_s.

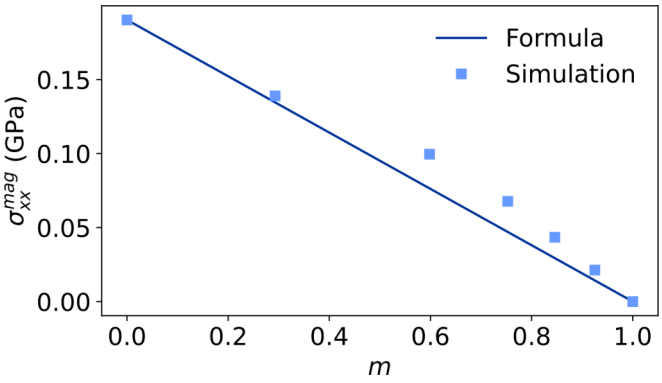

FIG. 8. Magnetic contribution to stress: Comparison of simulation data (squares) and the result obtained from theoretical Eq. (B10) (line). Here spontaneous volume magnetostriction in Eq. (B10) is taken as $\omega_s = 0.001$ the same as initial value of it in simulation.

We additionally note that although Eq. (B11) uses an approximately constant value of ω_s, and at the same time it agrees quite well with the simulation data (see Fig. 8), in the general case spontaneous volume magnetostriction also changes with temperature, as discussed in Appendix C.

APPENDIX C: TEMPERATURE DEPENDENCE OF SPONTANEOUS VOLUME MAGNETOSTRICTION

Spontaneous volume magnetostriction varies with temperature, decreasing up to zero at the Curie temperature reaching. As an example of such a temperature dependence, we present here the data from work [42] and compare them with the results obtained within the framework of our model from the simulations in LAMMPS (see Fig. 9). We consider a spin-lattice model with $\omega_s = -0.0012$ at $T = 0$ K, as in Ref. [42], by setting the Bethe-Slater parameters to $\alpha = 11.8227$ meV,

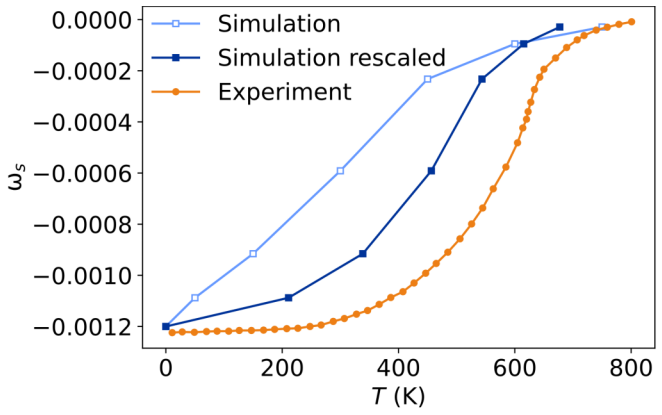

FIG. 9. Temperature dependence of the spontaneous volume magnetostriction. Experimental data are taken from Ref. [42]. The simulation curve is obtained from the simulations (with the corresponding to the experiment initial parameter $\omega_s = -0.0012$ at $T = 0$ K for FM case) as $\omega_s(T) = (V_{\mathrm{FM}}(T) - V_{\mathrm{PM}}(T))/V_{\mathrm{PM}}(T)$ while the simulation rescaled curve additionally takes into account the difference between the temperature in the simulation and the temperature in the experiment according to Eq. (10), based on Evans *et al.* [25].

$\gamma = 0.22358$, $\delta = 2.48901$ Å, and $R_c = 2.6$ Å. We see that better agreement between simulation and Ref. [42] is achieved by rescaling simulation temperature according to Eq. (10), suggesting that the method of Evans *et al.* [25] might also be useful for a quantitative simulation of the temperature dependence of $\omega_s(T)$. More advanced spin-lattice models, capable of accounting for possible thermal anomalies, could be developed through a genetic algorithm [65].

[1] M. Mattern, A. von Reppert, S. P. Zeuschner, M. Herzog, J.-E. Pudell, and M. Bargheer, Concepts and use cases for picosecond ultrasonics with x-rays, Photoacoustics **31**, 100503 (2023).

[2] M. Kobecki, G. Tandoi, E. Di Gaetano, M. Sorel, A. V. Scherbakov, T. Czerniuk, C. Schneider, M. Kamp, S. Höfling, A. V. Akimov, and M. Bayer, Picosecond ultrasonics with miniaturized semiconductor lasers, Ultrasonics **106**, 106150 (2020).

[3] O. Matsuda, M. C. Larciprete, R. Li Voti, and O. B. Wright, Fundamentals of picosecond laser ultrasonics, Ultrasonics **56**, 3 (2015).

[4] T. Saito, O. Matsuda, and O. B. Wright, Picosecond acoustic phonon pulse generation in nickel and chromium, Phys. Rev. B **67**, 205421 (2003).

[5] C. Thomsen, H. T. Grahn, H. J. Maris, and J. Tauc, Surface generation and detection of phonons by picosecond light pulses, Phys. Rev. B **34**, 4129 (1986).

[6] D. Schick, A. Bojahr, M. Herzog, R. Shayduk, C. von Korff Schmising, and M. Bargheer, UDKM1DSIM–A simulation toolkit for 1D ultrafast dynamics in condensed matter, Comput. Phys. Commun. **185**, 651 (2014).

[7] D. Schick, UDKM1DSIM–A Python toolbox for simulating 1D ultrafast dynamics in condensed matter, Comput. Phys. Commun. **266**, 108031 (2021).

[8] T. A. Ostler, J. Barker, R. F. L. Evans, R. W. Chantrell, U. Atxitia, O. Chubykalo-Fesenko, S. El Moussaoui, L. Le Guyader, E. Mengotti, L. J. Heyderman, F. Nolting, A. Tsukamoto, A. Itoh, D. Afanasiev, B. A. Ivanov, A. M. Kalashnikova, K. Vahaplar, J. Mentink, A. Kirilyuk, T. Rasing, and A. V. Kimel, Ultrafast heating as a sufficient stimulus for magnetization reversal in a ferrimagnet, Nat. Commun. **3**, 666 (2012).

[9] A. Kirilyuk, A. V. Kimel, and T. Rasing, Ultrafast optical manipulation of magnetic order, Rev. Mod. Phys. **82**, 2731 (2010).

[10] E. Beaurepaire, J.-C. Merle, A. Daunois, and J.-Y. Bigot, Ultrafast spin dynamics in ferromagnetic nickel, Phys. Rev. Lett. **76**, 4250 (1996).

[11] G. P. Zhang and W. Hübner, Laser-induced ultrafast demagnetization in ferromagnetic metals, Phys. Rev. Lett. **85**, 3025 (2000).

[12] S. N. Panda, S. Mondal, S. Majumder, and A. Barman, Ultrafast demagnetization and precession in permalloy films with varying thickness, Phys. Rev. B **108**, 144421 (2023).

[13] A. Lord, Thermal expansion due to spin waves at low temperatures, J. Phys. Chem. Solids **28**, 517 (1967).

[14] M. Mattern, J.-E. Pudell, G. Laskin, A. von Reppert, and M. Bargheer, Analysis of the temperature- and fluence-dependent magnetic stress in laser-excited $SrRuO_3$, Struct. Dyn. **8**, 024302 (2021).

[15] J. Pudell, A. von Reppert, D. Schick, F. Zamponi, M. Rössle, M. Herzog, H. Zabel, and M. Bargheer, Ultrafast negative thermal expansion driven by spin disorder, Phys. Rev. B **99**, 094304 (2019).

[16] P.-W. Ma, C. H. Woo, and S. L. Dudarev, Large-scale simulation of the spin-lattice dynamics in ferromagnetic iron, Phys. Rev. B **78**, 024434 (2008).

[17] J. Tranchida, S. Plimpton, P. Thibaudeau, and A. Thompson, Massively parallel symplectic algorithm for coupled magnetic spin dynamics and molecular dynamics, J. Comput. Phys. **372**, 406 (2018).

[18] K.-H. Yang and J. O. Hirschfelder, Generalizations of classical Poisson brackets to include spin, Phys. Rev. A **22**, 1814 (1980).

[19] S. Nikolov, M. A. Wood, A. Cangi, J.-B. Maillet, M.-C. Marinica, A. P. Thompson, M. P. Desjarlais, and J. Tranchida, Data-driven magneto-elastic predictions with scalable classical spin-lattice dynamics, npj Comput. Mater. **7**, 153 (2021).

[20] S. Nosé, A unified formulation of the constant temperature molecular dynamics methods, J. Chem. Phys. **81**, 511 (1984).

[21] B. Todd and P. Daivis, *Nonequilibrium Molecular Dynamics: Theory, Algorithms and Applications* (Cambridge University Press, Cambridge, 2017).

[22] A. V. Ruban, S. Khmelevskyi, P. Mohn, and B. Johansson, Temperature-induced longitudinal spin fluctuations in Fe and Ni, Phys. Rev. B **75**, 054402 (2007).

[23] M. Acet, E. F. Wassermann, K. Andersen, A. Murani, and O. Schärpff, The anomalous temperature dependence of the paramagnetic response of Fe-rich fcc Fe-Ni, Europhys. Lett. **40**, 93 (1997).

[24] F. Körmann, P.-W. Ma, S. L. Dudarev, and J. Neugebauer, Impact of magnetic fluctuations on lattice excitations in fcc nickel, J. Phys.: Condens. Matter **28**, 076002 (2016).

[25] R. F. L. Evans, U. Atxitia, and R. W. Chantrell, Quantitative simulation of temperature-dependent magnetization dynamics and equilibrium properties of elemental ferromagnets, Phys. Rev. B **91**, 144425 (2015).

[26] P.-W. Ma and S. L. Dudarev, Longitudinal magnetic fluctuations in Langevin spin dynamics, Phys. Rev. B **86**, 054416 (2012).

[27] P.-W. Ma, S. Dudarev, and C. Woo, SPILADY: A parallel CPU and GPU code for spin–lattice magnetic molecular dynamics simulations, Comput. Phys. Commun. **207**, 350 (2016).

[28] P.-W. Ma, S. L. Dudarev, and C. H. Woo, Spin-lattice-electron dynamics simulations of magnetic materials, Phys. Rev. B **85**, 184301 (2012).

[29] Y. Mishin, D. Farkas, M. J. Mehl, and D. A. Papaconstantopoulos, Interatomic potentials for monoatomic metals from experimental data and *ab initio* calculations, Phys. Rev. B **59**, 3393 (1999).

[30] S. Chikazumi, *Physics of Ferromagnetism* (Oxford University Press, Oxford, 2009).

[31] P. Nieves, J. Tranchida, S. Arapan, and D. Legut, Spin-lattice model for cubic crystals, Phys. Rev. B **103**, 094437 (2021).

[32] F. D. Murnaghan, The compressibility of media under extreme pressures, Proc. Natl. Acad. Sci. USA **30**, 244 (1944).

[33] C. L. Fu and K. M. Ho, First-principles calculation of the equilibrium ground-state properties of transition metals: Applications to Nb and Mo, Phys. Rev. B **28**, 5480 (1983).

[34] R. O'Handley, *Modern Magnetic Materials: Principles and Applications* (Wiley, New York, 1999).

[35] S. Zhang and R. Zhang, AELAS: Automatic ELAStic property derivations via high-throughput first-principles computation, Comput. Phys. Commun. **220**, 403 (2017).

[36] G. Alers, J. Neighbours, and H. Sato, Temperature dependent magnetic contributions to the high field elastic constants of nickel and an Fe-Ni alloy, J. Phys. Chem. Solids **13**, 40 (1960).

[37] P. Nieves, S. Arapan, S. Zhang, A. Kadzielawa, R. Zhang, and D. Legut, Automated calculations of exchange magnetostriction, Comput. Mater. Sci. **224**, 112158 (2023).

[38] J. F. Janak and A. R. Williams, Giant internal magnetic pressure and compressibility anomalies, Phys. Rev. B **14**, 4199 (1976).

[39] C. Williams, Thermal expansion and the ferromagnetic change in volume of nickel, Phys. Rev. **46**, 1011 (1934).

[40] M. Shimizu, Forced magnetostriction, magnetic contributions to bulk modulus and thermal expansion and pressure dependence of Curie temperature in iron, cobalt and nickel, J. Phys. Soc. Jpn. **44**, 792 (1978).

[41] F. Richter and U. Lotter, On the volume magnetostriction of nickel, iron, and cobalt, Phys. Status Solidi B **34**, K149 (1969).

[42] E. du Tremolet de Lacheisserie and J. Rouchy, The magnetoelastic coupling in nickel, J. Magn. Magn. Mater. **28**, 77 (1982).

[43] S. Mankovsky, D. Ködderitzsch, G. Woltersdorf, and H. Ebert, First-principles calculation of the Gilbert damping parameter via the linear response formalism with application to magnetic transition metals and alloys, Phys. Rev. B **87**, 014430 (2013).

[44] K. Schwarz, P. Mohn, P. Blaha, and J. Kubler, Electronic and magnetic structure of bcc Fe-Co alloys from band theory, J. Phys. F **14**, 2659 (1984).

[45] R. F. L. Evans, W. J. Fan, P. Chureemart, T. A. Ostler, M. O. A. Ellis, and R. W. Chantrell, Atomistic spin model simulations of magnetic nanomaterials, J. Phys.: Condens. Matter **26**, 103202 (2014).

[46] U. Atxitia, O. Chubykalo-Fesenko, J. Walowski, A. Mann, and M. Münzenberg, Evidence for thermal mechanisms in laser-induced femtosecond spin dynamics, Phys. Rev. B **81**, 174401 (2010).

[47] J. Mendil, P. Nieves, O. Chubykalo-Fesenko, J. Walowski, T. Santos, S. Pisana, and M. Münzenberg, Resolving the role of femtosecond heated electrons in ultrafast spin dynamics, Sci. Rep. **4**, 3980 (2014).

[48] M. Shalaby, A. Donges, K. Carva, R. Allenspach, P. M. Oppeneer, U. Nowak, and C. P. Hauri, Coherent and incoherent ultrafast magnetization dynamics in 3*d* ferromagnets driven by extreme terahertz fields, Phys. Rev. B **98**, 014405 (2018).

[49] P. Nieves, D. Serantes, and O. Chubykalo-Fesenko, Self-consistent description of spin-phonon dynamics in ferromagnets, Phys. Rev. B, **94**, 014409 (2016).

[50] G. Bertotti, I. D. Mayergoyz, and C. Serpico, *Nonlinear Magnetization Dynamics in Nanosystems* (Elsevier, Oxford, 2009).

[51] M. Pankratova, I. P. Miranda, D. Thonig, M. Pereiro, E. Sjöqvist, A. Delin, O. Eriksson, and A. Bergman, Heat-conserving three-temperature model for ultrafast demagnetization in nickel, Phys. Rev. B **106**, 174407 (2022).

[52] M. Pankratova, I. P. Miranda, D. Thonig, M. Pereiro, E. Sjöqvist, A. Delin, P. Scheid, O. Eriksson, and A. Bergman, Coupled atomistic spin-lattice simulations of ultrafast demagnetization in 3d ferromagnets, Sci. Rep. **14**, 8138 (2024).

[53] B. Koopmans, G. Malinowski, F. Dalla Longa, D. Steiauf, M. Fähnle, T. Roth, M. Cinchetti, and M. Aeschlimann, Explaining the paradoxical diversity of ultrafast laser-induced demagnetization, Nat. Mater. **9**, 259 (2010).

[54] U. Atxitia and O. Chubykalo-Fesenko, Ultrafast magnetization dynamics rates within the Landau-Lifshitz-Bloch model, Phys. Rev. B **84**, 144414 (2011).

[55] A. Stukowski, Visualization and analysis of atomistic simulation data with OVITO–the open visualization tool, Modell. Simul. Mater. Sci. Eng. **18**, 015012 (2010).

[56] C. Léveillé, K. Desjardins, H. Popescu, B. Vondungbo, M. Hennes, R. Delaunay, E. Jal, D. De Angelis, M. Pancaldi, E. Pedersoli, F. Capotondi, and N. Jaouen, Single-shot experiments at the soft X-FEL FERMI using a back-side-illuminated scientific CMOS detector, J. Synchrotron Radiat. **29**, 103 (2022).

[57] M. Schneider, B. Pfau, C. M. Günther, C. von Korff Schmising, D. Weder, J. Geilhufe, J. Perron, F. Capotondi, E. Pedersoli, M. Manfredda, M. Hennecke, B. Vodungbo, J. Lüning, and S. Eisebitt, Ultrafast demagnetization dominates fluence dependence of magnetic scattering at Co *M* edges, Phys. Rev. Lett. **125**, 127201 (2020).

[58] V. Cardin, T. Balciunas, K. Légaré, A. Baltuska, H. Ibrahim, E. Jal, B. Vodungbo, N. Jaouen, C. Varin, J. Lüning, and F. Légaré, Wavelength scaling of ultrafast demagnetization in Co/Pt multilayers, Phys. Rev. B **101**, 054430 (2020).

[59] H.-T. Chang, A. Guggenmos, S. K. Cushing, Y. Cui, N. U. Din, S. R. Acharya, I. J. Porter, U. Kleineberg, V. Turkowski, T. S. Rahman, D. M. Neumark, and S. R. Leone, Electron thermalization and relaxation in laser-heated nickel by few-femtosecond core-level transient absorption spectroscopy, Phys. Rev. B **103**, 064305 (2021).

[60] K. J. Kapcia, V. Tkachenko, F. Capotondi, A. Lichtenstein, S. Molodtsov, L. Müller, A. Philippi-Kobs, P. Piekarz, and B. Ziaja, Modeling of ultrafast x-ray induced magnetization dynamics in magnetic multilayer systems, npj Comput. Mater. **8**, 212 (2022).

[61] K. J. Kapcia, V. Tkachenko, F. Capotondi, A. Lichtenstein, S. Molodtsov, L. Mueller, A. Philippi-Kobs, P. Piekarz, and B. Ziaja, Electronic processes occurring during ultrafast demagnetization of cobalt triggered by x-ray photons tuned to the co L_3 resonance, Phys. Rev. B **107**, 094402 (2023).

[62] E. D. T. de Lacheisserie, *Magnetostriction: Theory and Application of Magnetoelasticity* (CRC Press, Boca Raton, FL, 1993).

[63] J. R. Cooke and J. R. Lukes, Angular momentum conservation in spin-lattice dynamics simulations, Phys. Rev. B **107**, 024419 (2023).

[64] Z. Zheng, Q. Zheng, and J. Zhao, Spin-orbit coupling induced demagnetization in Ni: *Ab initio* nonadiabatic molecular dynamics perspective, Phys. Rev. B **105**, 085142 (2022).

[65] S. Nikolov, P. Nieves, A. P. Thompson, M. A. Wood, and J. Tranchida, Temperature dependence of magnetic anisotropy and magnetoelasticity from classical spin-lattice calculations, Phys. Rev. B **107**, 094426 (2023).